Strongly Overdamped Dissipative Particle Dynamics for Fluid-Solid Systems

N. Phan-Thien[1], N. Mai-Duy[1,2,*], B.C. Khoo[1], and D. Duong-Hong[3]

[1]Department of Mechanical Engineering, Faculty of Engineering,
National University of Singapore, Singapore.
[2]Computational Engineering and Science Research Centre,
School of Mechanical and Electrical Engineering,
University of Southern Queensland, Toowoomba, QLD 4350, Australia.
[3]Welch Allyn Singapore Pte. Ltd.,
438B Alexandra Road, #01-03 Alexandra Technopark, Singapore 119968

Submitted to *Applied Mathematical Modelling*, 5/Feb/2015; revised, 8/Nov/2015; revised (2), 4/Dec/2015

Abstract In this paper, a numerical scheme is used to study strongly-overdamped Dissipative Particles Dynamics (DPD) systems for the modelling of fluid-solid systems. In the scheme, the resultant set of algebraic equations for the velocities are directly solved in an iterative manner. Different test problems, e.g., viscometric flows, particulate suspensions and flows past a periodic square array of cylinders, are used to verify the proposed method. In the simulation of particulate suspensions, a new simple model for massless suspended particles is presented. A DPD fluid in the overdamped limit is shown to possess several attractive properties including much faster dynamic response and near-incompressibility.

Keywords: Dissipative Particles Dynamics, strongly overdamped systems, compressibility, dynamic response, particulate suspension

*Corresponding author: E-mail nam.mai-duy@usq.edu.au, Telephone +61-7-4631-2748, Fax +61-7-4631 2526

1 Introduction

Dissipative Particles Dynamics (DPD) is a particle-based method originally designed for the simulation of complex fluids on mesoscopic length scale [1-5]. In DPD, a fluid is modelled by a system of particles interacting with each others through pairwise forces. These particles are supposed to model the fluid behaviour (viscous, or otherwise dictated by the specification of the microstructure connectivity) when seen in a representative volume. Objects suspended in the fluid, e.g., rigid particles and droplets, can also be represented by DPD particles with appropriate forms of interactions. These features make the DPD method (and its variants) very attractive in the modelling of complex fluid systems. DPD has been used with varying degrees of success to simulate various problems: particulate suspensions, emulsions, polymer solutions, polymer melts, red blood cell modelling, etc.

In [6], the equivalent Poisson ratio of a DPD fluid (a measure of compressibility) in the absence of conservative forces was estimated as 0.24, and measured in a simulated four-rolled mill at a value of 0.48 (at best), less than the incompressible limit of 0.5. This compressibility nature of a DPD fluid implies that unwanted effects due to compressibility of a DPD flow will occur, and special care is needed in interpretation of the flow results, especially at high Re number. The Mach number, which is the ratio of a characteristic velocity of the fluid to its sonic velocity, can also be used to estimate the effects of compressibility. The fluid flow may be considered weakly compressible (or nearly incompressible) when the flow Mach number is less than 0.3. Another past issue is the Schmidt number, the ratio of the diffusion of momentum to the diffusion of mass in a fluid, governing the dynamic response of a fluid. For a standard-parameter DPD fluid, the Schmidt number is of the order unity. For a real water-like fluid, the Schmidt number is $O(10^3)$, and there is the need to improve on the dynamic behaviour of the DPD system. By some slight modifications to its standard parameters, a DPD fluid could be designed to have a Schmidt number of $O(10^3)$ [7].

The Reynolds (Re), Mach (M) and Schmidt (Sc) numbers are defined as [5]

$$Re = \frac{mnUL}{\eta}; \quad M = \frac{U}{c_s},\ c_s^2 = \frac{k_B T}{m} + \frac{\pi}{15}\frac{anr_c^4}{m}; \quad Sc = \frac{\eta}{mnD}, \tag{1}$$

where U is a flow characteristic velocity, L a flow characteristic length, m the mass of the particle, n the number density, η the dynamic viscosity, c_s the speed of sound, k_BT the Boltzmann temperature (mean kinetic energy of the particles), a the repulsion coefficient, r_c the cut-off radius for the particles interactions, and D the fluid diffusion coefficient. It is therefore possible to control the three quantities Re, M and Sc collectively by means of m. A strongly overdamped system results with the limit of $m \to 0$; the limit corresponds to $Re \to 0$, $M \to 0$ and $Sc \to \infty$. This limit also corresponds to the inertial time scale $m\gamma^{-1} \to 0$ (γ the coefficient characterising the strength of the dissipative force, refer to (3) below). It is noted that highly overdamped Brownian dynamics systems and their behaviour have been extensively studied and well established, but no such studies exist for overdamped DPD systems. In [8,9], the use of low mass was proposed in the DPD modelling of slow (creeping) flow in which high sonic speed, low Reynolds and high Schmidt numbers are achieved altogether. This comes at the expense of solving stiff stochastic differential equations for which exponential time differencing (ETD) schemes may be more efficient than standard solvers. In [10], the overdamped limit for a simple DPD system was investigated, where DPD particles are of the same type and the imposed boundary conditions are all periodic. The resultant system matrix has zero row and zero column sums, corresponding to a loss of second-order time derivatives, and a multiplicity of solutions (each solution differs from the other by a rigid-body motion). It was shown that a possible and practical iterative solution scheme is to add to the original system the eigenvectors weighted by the inner product formed from the eigenvectors and the solution vector (which is in fact the constraint of zero center of mass velocity) - this later step was recognised as a Wielandt's deflation technique.

The present work is an extension of our previous study of strongly-overdamped DPD, with included movable and stationary solid bodies, also modelled using a subset of DPD particles. It will be shown that the velocity constraints on stationary particles render a unique solution to the system without the need for Wielandt's deflation. Emphasis will be placed on: (i) the effects of using frozen particles on the flow; (ii) the effects of including physical constraint of constant velocity of the mass centre in the DPD system; and (iii) the modelling of massless suspended particles. Basic DPD equations in the overdamped limit are given in Section 2. The proposed numerical procedure is presented in Section 3 and then verifications are given

in Section 4. Section 5 gives some concluding remarks.

2 DPD equations for strongly overdamped systems

The DPD equations can be written as

$$\frac{d\mathbf{r}_i}{dt} = \mathbf{v}_i, \tag{2}$$

$$m_i \frac{d\mathbf{v}_i}{dt} = \sum_{j=1, j\neq i}^{N} a_{ij} w_C \mathbf{e}_{ij} - \sum_{j=1, j\neq i}^{N} \gamma w_D \left(\mathbf{e}_{ij} \cdot \mathbf{v}_{ij}\right) \mathbf{e}_{ij} + \sum_{j=1, j\neq i}^{N} \sigma w_R \theta_{ij} \mathbf{e}_{ij}, \tag{3}$$

where $i = (1, 2, \cdots, N)$, N is the number of particles, m_i, $\mathbf{r}_i$ and $\mathbf{v}_i$ the mass, position and velocity vector of the ith particle, t the time, $\mathbf{v}_{ij} = \mathbf{v}_i - \mathbf{v}_j$, $\mathbf{e}_{ij} = \mathbf{r}_{ij}/r_{ij}$ ($\mathbf{r}_{ij} = \mathbf{r}_i - \mathbf{r}_j$, $r_{ij} = |\mathbf{r}_{ij}|$), a_{ij}, γ and σ are constant parameters, w_C, w_D and w_R are the weight functions that vanish if $r_{ij} \geq r_c$, and θ_{ij} a Gaussian white noise ($\theta_{ij} = \theta_{ji}$) with stochastic properties

$$\langle \theta_{ij} \rangle = 0, \tag{4}$$

$$\langle \theta_{ij}(t) \theta_{kl}(t') \rangle = \left(\delta_{ik}\delta_{jl} + \delta_{il}\delta_{jk}\right) \delta\left(t - t'\right), \text{with } i \neq k \text{ and } j \neq l. \tag{5}$$

The first term on the right side of (3) is the conservative force ($\mathbf{F}_{ij,C}$), the second the dissipative force ($\mathbf{F}_{ij,D}$) and the last the random force ($\mathbf{F}_{ij,R}$). The equilibrium and detailed balance (Fluctuation-Dissipation theorem, [2]) of the system requires

$$w_D(r_{ij}) = \left(w_R(r_{ij})\right)^2, \tag{6}$$

$$k_B T = \frac{\sigma^2}{2\gamma}, \tag{7}$$

where $k_B T$ is the Boltzmann temperature (mean kinetic energy of the particles). In this study, we take the weighting functions in the form $w_C(r_{ij}) = 1 - r_{ij}/r_c$ and $w_D(r_{ij}) = (1 - r_{ij}/r_c)^{1/2}$. It is noted that the exponent in the expression for w_D is taken to be 1/2 instead of 2 to increase the Sc number by a factor of 10 and thereby improve on the dynamic response of the DPD fluid [7]. The DPD forces are centre-to-centre and thus both linear momentum and angular momentum are conserved strictly. Furthermore, owing to the fact

that DPD particles interact through a soft potential, the simulation can be carried out on length and time scales far beyond those associated with molecular dynamics (MD). Viscous interactions are accounted for by dissipative forces depending on the relative velocity of the particle.

Calculation of mean quantities

The flow domain is divided into bins which are used to collect local data. The assuming-ergodic flow properties are calculated by time averaging over all sampled data in each bin.

The fluid density and linear momentum are, respectively, defined as

$$\rho(\mathbf{r},t) = \left\langle \sum_i m\delta(\mathbf{r}-\mathbf{r}_i) \right\rangle, \tag{8}$$

$$\rho(\mathbf{r},t)\mathbf{u} = \left\langle \sum_j m\mathbf{v}_j\delta(\mathbf{r}-\mathbf{r}_j) \right\rangle. \tag{9}$$

The stress tensor is found for a microscopic system of particles by the Irving-Kirkwood method

$$\mathbf{T} = -n\left\langle \sum_i m\mathbf{V}_i\mathbf{V}_i + \frac{1}{2}\sum_i\sum_{j\neq i}\mathbf{r}_{ij}\left(\mathbf{F}_{ij,C}+\mathbf{F}_{ij,D}\right) \right\rangle, \tag{10}$$

where $\mathbf{V}_i = \mathbf{v}_i - \mathbf{u}$ is the peculiar velocity of particle i with respect to the mean field velocity $\mathbf{u}$ and $\langle . \rangle$ denotes the ensemble average. The sums on the right side of (10) denote the contributions to the stress from the momentum transfer of DPD particles and from the interaction forces, respectively. The pressure can be defined as the trace of the stress tensor

$$p = -\frac{1}{3}\mathrm{tr}\ \mathbf{T}. \tag{11}$$

It is noted that these mean quantities satisfy conservation laws:

$$\frac{\partial}{\partial t}\rho\left(\mathbf{r},t\right) + \nabla\cdot\left(\rho\left(\mathbf{r},t\right)\mathbf{u}\left(\mathbf{r},t\right)\right) = 0, \qquad \nabla = \partial/\partial\mathbf{r}, \tag{12}$$

and

$$\frac{\partial}{\partial t}\left(\rho\mathbf{u}\right) + \nabla\cdot\left(\rho\mathbf{u}\mathbf{u}\right) = \nabla\cdot\mathbf{T}. \tag{13}$$

Thus, DPD may be regarded as a particle-based method for solving continuum flow problems

(12)-(13). Adopting this particle-based point of view, DPD particles may be thought of as a model of a behaviour (e.g., viscous compressible fluid), not merely particles of some exclusion sizes. More details can be found in [5,11], for instance.

Strongly overdamped DPD systems: In the overdamped limit ($m/\gamma^2 \to 0$), equation (3) reduces to a balance of forces

$$\sum_{j=1,j\neq i}^{N} \gamma w_D \mathbf{e}_{ij}\mathbf{e}_{ij} \cdot (\mathbf{v}_i - \mathbf{v}_j) = \sum_{j=1,j\neq i}^{N} a_{ij} w_C \mathbf{e}_{ij} + \sum_{j=1,j\neq i}^{N} \sigma w_R \theta_{ij} \mathbf{e}_{ij}. \tag{14}$$

3 Proposed numerical procedure

Consider a DPD system as shown in Figure 1. In the wall regions, as represented by two boxes, top and bottom, the wall particles, numbered N_w, are frozen. We can arbitrarily number the DPD particles consecutively as $i = 1, \ldots, N_s, N_s + 1, \ldots, N$, where N_s is the number of DPD particles representing the fluid (the solvent), and $N = N_s + N_w$ the total number of DPD particles. Initially, the fluid particles are distributed uniformly, and their velocities are generated randomly with a zero sum in all directions.

We construct the DPD system by letting i taking values from 1 to N_s in (14)

$$\mathcal{A}\mathbf{v} = \mathbf{f}, \tag{15}$$

where $\mathcal{A}$ is the system matrix, $\mathbf{v}$ the column vector of unknown velocity vectors and $\mathbf{f}$ the column vector of right hand force vectors and part of the original left hand matrix multiplied by known velocity vectors:

$$\mathcal{A} = \begin{bmatrix} \sum_{j=2}^{N} \gamma w_D \mathbf{e}_{1j}\mathbf{e}_{1j} & -\gamma w_D \mathbf{e}_{12}\mathbf{e}_{12} & \cdots & -\gamma w_D \mathbf{e}_{1N_s}\mathbf{e}_{1N_s} \\ -\gamma w_D \mathbf{e}_{21}\mathbf{e}_{21} & \sum_{j=1,j\neq 2}^{N} \gamma w_D \mathbf{e}_{2j}\mathbf{e}_{2j} & \cdots & -\gamma w_D \mathbf{e}_{2N_s}\mathbf{e}_{2N_s} \\ \vdots & \vdots & \ddots & \vdots \\ -\gamma w_D \mathbf{e}_{N_s1}\mathbf{e}_{N_s1} & -\gamma w_D \mathbf{e}_{N_s2}\mathbf{e}_{N_s2} & \cdots & \sum_{j=1}^{N-1} \gamma w_D \mathbf{e}_{N_sj}\mathbf{e}_{N_sj} \end{bmatrix}, \tag{16}$$

$$\mathbf{v} = (\mathbf{v}_1, \mathbf{v}_2, \cdots, \mathbf{v}_{N_s})^T, \tag{17}$$

$$\mathbf{f} = \begin{pmatrix} \sum_{j=2}^{N} a_{1j} w_C \mathbf{e}_{1j} + \sum_{j=2}^{N} \sigma w_R \theta_{1j} \mathbf{e}_{1j} \\ \sum_{j=1,j\neq 2}^{N} a_{2j} w_C \mathbf{e}_{2j} + \sum_{j=1,j\neq 2}^{N} \sigma w_R \theta_{2j} \mathbf{e}_{2j} \\ \vdots \\ \sum_{j=1}^{N-1} a_{N_s j} w_C \mathbf{e}_{N_s j} + \sum_{j=1}^{N-1} \sigma w_R \theta_{N_s j} \mathbf{e}_{N_s j} \end{pmatrix} + \begin{pmatrix} \sum_{j=N_s+1}^{N} \gamma w_D \mathbf{e}_{1j} \mathbf{e}_{1j} \mathbf{v}_j \\ \sum_{j=N_s+1}^{N} \gamma w_D \mathbf{e}_{2j} \mathbf{e}_{2j} \mathbf{v}_j \\ \vdots \\ \sum_{j=N_s+1}^{N} \gamma w_D \mathbf{e}_{N_s j} \mathbf{e}_{N_s j} \mathbf{v}_j \end{pmatrix}. \quad (18)$$

Since the known velocity vectors, corresponding to the wall particles, on the left side of (14) are moved to the right side (the last term in (18)), the row and column sums of the system matrix $\mathcal{A}$ are no longer zero and consequently, the problem of multiple solutions due to a rigid-body motion is no longer a concern. It can be seen that $\mathcal{A}$ is a sparse matrix because the construction of rows of this matrix involves only particles within the interaction zone. Below are two iterative schemes for solving the system $\mathcal{A}\mathbf{v} = \mathbf{f}$. They are applicable for 2D and 3D space. In Scheme 2, the Wielandt's deflation method is utilised to reduce the spectral radius (faster convergence). In this regard, Scheme 2 is expected to be more efficient than Scheme 1.

3.1 Scheme 1

We decompose the system (15) into

$$\mathcal{I}\mathbf{v} + \mathcal{K}\mathbf{v} = \mathbf{f}, \quad (19)$$

where

$$\mathcal{I} = \begin{bmatrix} \sum_{j=2}^{N} \gamma w_D \mathbf{e}_{1j} \mathbf{e}_{1j} & \mathbf{0} & \cdots & \mathbf{0} \\ \mathbf{0} & \sum_{j=1,j\neq 2}^{N} \gamma w_D \mathbf{e}_{2j} \mathbf{e}_{2j} & \cdots & \mathbf{0} \\ \vdots & \vdots & \ddots & \vdots \\ \mathbf{0} & \mathbf{0} & \cdots & \sum_{j=1}^{N-1} \gamma w_D \mathbf{e}_{N_s j} \mathbf{e}_{N_s j} \end{bmatrix}, \quad (20)$$

and

$$\mathcal{K} = \begin{bmatrix} \mathbf{0} & -\gamma w_D \mathbf{e}_{12} \mathbf{e}_{12} & \cdots & -\gamma w_D \mathbf{e}_{1N_s} \mathbf{e}_{1N_s} \\ -\gamma w_D \mathbf{e}_{21} \mathbf{e}_{21} & \mathbf{0} & \cdots & -\gamma w_D \mathbf{e}_{2N_s} \mathbf{e}_{2N_s} \\ \vdots & \vdots & \ddots & \vdots \\ -\gamma w_D \mathbf{e}_{N_s 1} \mathbf{e}_{N_s 1} & -\gamma w_D \mathbf{e}_{N_s 2} \mathbf{e}_{N_s 2} & \cdots & \mathbf{0} \end{bmatrix}. \quad (21)$$

The inverse of $\mathcal{I}$ can be computed in the following form

$$\mathcal{I}^{-1} = \begin{bmatrix} \left(\sum_{j=2}^{N} \gamma w_D \mathbf{e}_{1j}\mathbf{e}_{1j}\right)^{-1} & \mathbf{0} & \cdots & 0 \\ \mathbf{0} & \left(\sum_{j=1,j\neq 2}^{N} \gamma w_D \mathbf{e}_{2j}\mathbf{e}_{2j}\right)^{-1} & \cdots & \mathbf{0} \\ \vdots & \vdots & \ddots & \vdots \\ \mathbf{0} & \mathbf{0} & \cdots & \left(\sum_{j=1}^{N-1} \gamma w_D \mathbf{e}_{N_s j}\mathbf{e}_{N_s j}\right)^{-1} \end{bmatrix}. \tag{22}$$

Multiplying both sides of (19) by $\mathcal{I}^{-1}$ results in

$$\mathbf{v} + \mathcal{H}\mathbf{v} = \mathbf{b}, \tag{23}$$

where $\mathcal{H} = \mathcal{I}^{-1}\mathcal{K}$ and $\mathbf{b} = \mathcal{I}^{-1}\mathbf{f}$. To solve (23), a simple Picard's iteration scheme can be used

$$\mathbf{v}_i^l = -\mathcal{H}_i \mathbf{v}^{l-1} + \mathbf{b}_i, \tag{24}$$

where $i = (1, 2, \cdots, N_s)$,

$$\mathcal{H}_i = \left(\sum_{j=1,j\neq i}^{N} \gamma w_D \mathbf{e}_{ij}\mathbf{e}_{ij}\right)^{-1} \left[-\gamma w_D \mathbf{e}_{i1}\mathbf{e}_{i1}, \cdots, -\gamma w_D \mathbf{e}_{i(i-1)}\mathbf{e}_{i(i-1)}, \mathbf{0}, -\gamma w_D \mathbf{e}_{i(i+1)}\mathbf{e}_{i(i+1)}, \cdots, -\gamma w_D \mathbf{e}_{iN_s}\mathbf{e}_{iN_s}\right], \tag{25}$$

and

$$\mathbf{b}_i = \left(\sum_{j=1,j\neq i}^{N} \gamma w_D \mathbf{e}_{ij}\mathbf{e}_{ij}\right)^{-1} \left(\sum_{j=1,j\neq i}^{N} a_{ij} w_C \mathbf{e}_{ij} + \sum_{j=1,j\neq i}^{N} \sigma w_R \theta_{ij}\mathbf{e}_{ij} + \sum_{j=N_s+1}^{N} \gamma w_D \mathbf{e}_{ij}\mathbf{e}_{ij}\mathbf{v}_j\right). \tag{26}$$

The iterative process stops when the following convergence measure is satisfied

$$norm(\mathbf{v}^l - \mathbf{v}^{l-1}) < 10^{-7} norm(\mathbf{v}^l), \tag{27}$$

where the notation *norm* is used to denote the Euclidean distance.

In addition to this, we need to integrate the velocities to advance the position of the particles.

A first-order Euler algorithm is employed here

$$\mathbf{r}_i^{k+1} = \mathbf{r}_i^k + \mathbf{v}_i^k \Delta t, \tag{28}$$

where $\Delta t = t^{k+1} - t^k$.

Now we investigate the effects of frozen particles in the wall regions on the flow. Consider the ith wall particle ($i = (N_s + 1, \cdots, N)$). Its motion is governed by

$$m\frac{d\mathbf{v}_i}{dt} = \sum_{j=1}^{N} (\mathbf{F}_{ij,C} + \mathbf{F}_{ij,D} + \mathbf{F}_{ij,R}) + \mathbf{F}_{i,W}, \tag{29}$$

where $\mathbf{F}_{i,W}$ is the constraint (reaction) force from the ground/base. Since the particle i is frozen ($\mathbf{v}_i = \mathbf{0}$), the constraint force on it is computed as

$$\mathbf{F}_{i,W} = -\sum_{j=1}^{N} (\mathbf{F}_{ij,C} + \mathbf{F}_{ij,D} + \mathbf{F}_{ij,R}). \tag{30}$$

The total force exerted on the DPD system from the base is thus given by

$$\widetilde{\mathbf{F}} = \sum_{i=N_s+1}^{N} \mathbf{F}_{i,W} = -\sum_{i=N_s+1}^{N}\sum_{j=1}^{N} (\mathbf{F}_{ij,C} + \mathbf{F}_{ij,D} + \mathbf{F}_{ij,R}) = \sum_{i=1}^{N_s}\sum_{j=1}^{N} (\mathbf{F}_{ij,C} + \mathbf{F}_{ij,D} + \mathbf{F}_{ij,R}). \tag{31}$$

It can be seen that the total force exerted on the fluid region from the walls is also $\widetilde{\mathbf{F}}$.

The centres of mass of the fluid interior and the wall particles are given by

$$mN_s\mathbf{R}_c^s = \sum_{i=1}^{N_s} m\mathbf{r}_i, \quad mN_w\mathbf{R}_c^w = \sum_{i=N_s+1}^{N} m\mathbf{r}_i. \tag{32}$$

Note that (i) the centre of mass of the whole DPD system is

$$N\mathbf{R}_c = N_s\mathbf{R}_c^s + N_w\mathbf{R}_c^w; \tag{33}$$

and (ii) the three centres are initially located at the origin with zero velocities.

In the present system, there are two types of forces, the DPD and reaction forces. The sum of DPD forces vanishes due to their pair-wise interactions, while the reaction forces,

which are forces exerted on the frozen forces from the ground/base, do not cancel out. As a result, the mass centre of the system/fluid region will not move at constant (zero) velocity any longer. Consider a domain of 10×10 in reduced units (10×12 if the two wall regions are included) as shown in Figure 1. We employ the standard DPD parameters: $a_{ij} = 18.5$, $n = 4$, $\sigma = 3$, $r_c = 1$ and $k_B T = 1$, and take $\Delta t = 0.005$. The number of particles in the fluid region are 400. In each wall region, there are two boundary layers on which 20 and 50 uniformly-distributed fixed particles are employed. The total number of particles used are thus 540. It is observed that (i) velocity components of the mass centre are oscillatory with zero mean and magnitude in the range of -15 to 15 for the x component and of -8 to 8 for the y component; (ii) the location of the mass centre moves far away from its original position and displacements in the x direction are much larger than in the y direction (for 2500 time steps, $-0.6 < x_{cm} < 1.2$ and $-0.1 < y_{cm} < 0.1$); and the total of reaction forces also fluctuates with zero mean. It appears that the reaction forces are transmitted into the fluid region, just like "external forces", producing some fluid motion, which is a consequential artefact of the wall constraints.

3.2 Scheme 2

In this scheme, the DPD system incorporates the physical constraint of constant velocity of the centre of mass in order to enhance the efficiency of the iterative solving process as well as to offset against the fluid motion induced by constraint forces.

We now introduce the relative motion of the particles

$$\mathbf{x}_i = \mathbf{r}_i - \mathbf{R}_c^s, \quad i = (1, \cdots, N_s). \tag{34}$$

Differentiating equation (34) with respect to time twice and making use of (3), (32), (30) and (31) yield

$$m\ddot{\mathbf{x}}_i = \sum_{j=1, j\neq i}^{N} (\mathbf{F}_{ij,C} + \mathbf{F}_{ij,D} + \mathbf{F}_{ij,R}) - \frac{1}{N_s}\widetilde{\mathbf{F}}. \tag{35}$$

This relative motion of fluid DPD particles (equivalent to describing the motion in a frame moving with the centre of mass), for which the DPD equations involve one more force term,

is now guaranteed to have their centre of mass in this moving frame stationary. It should be emphasised that the new force term in (35) is only present with wall particles, when a transmission of forces from the wall to the fluid region occurs. If there are no wall particles, these reaction forces are zero, and this mentioned force field vanishes. The sum of all forces exerted on the DPD system completely vanishes.

Let the fluid density and linear momentum in the moving frame, respectively, be defined as

$$\rho(\mathbf{x},t) = \left\langle \sum_i m\delta(\mathbf{x}-\mathbf{x}_i) \right\rangle, \tag{36}$$

$$\rho(\mathbf{x},t)\overline{\mathbf{u}} = \left\langle \sum_j m\dot{\mathbf{x}}_j\delta(\mathbf{x}-\mathbf{x}_j) \right\rangle. \tag{37}$$

Note that $\mathbf{r} = \mathbf{x} + \mathbf{R}_c^s$ and $\mathbf{r}_i = \mathbf{x}_i + \mathbf{R}_c^s$, and thus $\mathbf{r} - \mathbf{r}_i = \mathbf{x} - \mathbf{x}_i$. Equation (8) becomes

$$\rho(\mathbf{r},t) = \left\langle \sum_i m\delta(\mathbf{r}-\mathbf{r}_i) \right\rangle = \left\langle \sum_i m\delta(\mathbf{x}-\mathbf{x}_i) \right\rangle = \rho(\mathbf{x},t). \tag{38}$$

Note that $\mathbf{r} = \mathbf{x}+\mathbf{R}_c^s$ and $\mathbf{r}_j = \mathbf{x}_j+\mathbf{R}_c^s$, and thus $\mathbf{v}_j = \dot{\mathbf{x}}_j+\dot{\mathbf{R}}_c^s$ and $\mathbf{r}-\mathbf{r}_j = \mathbf{x}-\mathbf{x}_j$. Equation (9) becomes

$$\begin{aligned}
\rho(\mathbf{r},t)\mathbf{u} &= \left\langle \sum_j m\mathbf{v}_j\delta(\mathbf{r}-\mathbf{r}_j) \right\rangle \\
&= \left\langle \sum_j m\dot{\mathbf{x}}_j\delta(\mathbf{x}-\mathbf{x}_j) \right\rangle + \left\langle \sum_j m\dot{\mathbf{R}}_c^s\delta(\mathbf{r}-\mathbf{r}_j) \right\rangle \\
&= \rho(\mathbf{x},t)\overline{\mathbf{u}} + \left\langle \sum_j m\dot{\mathbf{R}}_c^s\delta(\mathbf{r}-\mathbf{r}_j) \right\rangle,
\end{aligned} \tag{39}$$

where the second term on the right side of (39) can be regarded as the side effect of freezing the wall particles. One expects this term to approach zero as the number of time steps used for the time averaging process increases (in the case when periodic boundary conditions are applied, this can be demonstrated to be zero). The velocity $\overline{\mathbf{u}}$ to be determined is the wanted part of the velocity $\mathbf{u}$.

Note that $\mathbf{r}_i = \mathbf{x}_i + \mathbf{R}_c^s$, $\mathbf{r}_j = \mathbf{x}_j + \mathbf{R}_c^s$, $\mathbf{v}_i = \dot{\mathbf{x}}_i + \dot{\mathbf{R}}_c^s$ and $\mathbf{u} = \overline{\mathbf{u}} + \langle\dot{\mathbf{R}}_c^s\rangle$, and thus $\mathbf{r}_{ij} = \mathbf{x}_{ij}$ and $\mathbf{V}_i = \mathbf{v}_i - \mathbf{u} = \overline{\mathbf{V}}_i + \left(\dot{\mathbf{R}}_c^s - \langle\dot{\mathbf{R}}_c^s\rangle\right)$, where $\overline{\mathbf{V}}_i = \dot{\mathbf{x}}_i - \overline{\mathbf{u}}$ is the peculiar velocity of particle

i in the relative motion. Equation (10) can be rewritten as

$$\begin{aligned}\mathbf{T} &= -n\left\langle \sum_i m\mathbf{V}_i\mathbf{V}_i + \frac{1}{2}\sum_i\sum_{j\neq i}\mathbf{r}_{ij}\left(\mathbf{F}_{ij,C}+\mathbf{F}_{ij,D}\right)\right\rangle, \\ &= -n\left\langle \sum_i m\overline{\mathbf{V}}_i\overline{\mathbf{V}}_i + \sum_i m\left(\dot{\mathbf{R}}_c^s - \langle\dot{\mathbf{R}}_c^s\rangle\right)\left(\dot{\mathbf{R}}_c^s - \langle\dot{\mathbf{R}}_c^s\rangle\right) + \frac{1}{2}\sum_i\sum_{j\neq i}\mathbf{x}_{ij}\left(\mathbf{F}_{ij,C}+\mathbf{F}_{ij,D}\right)\right\rangle.\end{aligned} \tag{40}$$

Owing to the facts that (i) $\dot{\mathbf{R}}_c^s - \langle\dot{\mathbf{R}}_c^s\rangle$ is not spatial dependent and (ii) only the pressure gradient (not the pressure itself) matters in the momentum balance equation, the stress tensor computed in the moving frame is in fact the stress tensor (10) modulo an un-important isotropic pressure term. Expressions (38), (39) and (40) are valid for any value of m.

With the presence of frozen wall particles, the motion of DPD particles in reference to the centre of mass is a better means of representation of the flow as the artefacts of the wall constraints are absent. The centre of mass of the present system has constant (zero) velocities. Hereafter, for the sake of simplicity, notations for the position, velocity, etc., in the moving frame are taken to be the same as those in the fixed frame. Furthermore, the DPD formulation can now be reformulated with the help of Wielandt's deflation method [12,13] to deflate the largest value of the eigenvalues of the matrix $\mathcal{H}$ and thus to reduce the spectral radius (faster convergence)

$$\mathbf{v} + \mathcal{H}\mathbf{v} + \boldsymbol{\epsilon}_x\left[\mathbf{v},\boldsymbol{\epsilon}_x\right] + \boldsymbol{\epsilon}_y\left[\mathbf{v},\boldsymbol{\epsilon}_y\right] + \boldsymbol{\epsilon}_z\left[\mathbf{v},\boldsymbol{\epsilon}_z\right] = \widetilde{\mathbf{b}}, \tag{41}$$

where $[\cdot,\cdot]$ denotes the natural inner product of two vector elements in the underlying space,

$$\boldsymbol{\epsilon}_x = \left(\mathbf{U}_x,\mathbf{U}_x,...,\mathbf{U}_x\right)^T/\sqrt{N_s}U_x,\ \mathbf{U}_x = (1,0,0)^T,\ U_x^2 = \mathbf{U}_x\cdot\mathbf{U}_x, \tag{42}$$

$$\boldsymbol{\epsilon}_y = \left(\mathbf{U}_y,\mathbf{U}_y,...,\mathbf{U}_y\right)^T/\sqrt{N_s}U_y,\ \mathbf{U}_y = (0,1,0)^T,\ U_y^2 = \mathbf{U}_y\cdot\mathbf{U}_y, \tag{43}$$

$$\boldsymbol{\epsilon}_z = \left(\mathbf{U}_z,\mathbf{U}_z,...,\mathbf{U}_z\right)^T/\sqrt{N_s}U_z,\ \mathbf{U}_z = (0,0,1)^T,\ U_z^2 = \mathbf{U}_z\cdot\mathbf{U}_z, \tag{44}$$

and

$$\widetilde{\mathbf{b}} = \mathbf{b} + \mathcal{I}^{-1}(\underbrace{-\frac{1}{N_s}\widetilde{\mathbf{F}},\cdots,-\frac{1}{N_s}\widetilde{\mathbf{F}}}_{N_s})^T. \tag{45}$$

The last three terms on the left of (41) represent the constraint of zero velocity of the centre of mass [10] and therefore they do not contribute to the governing equation.

To solve (41), a simple Picards iteration scheme can be used

$$\mathbf{v}_i^l = -\mathcal{H}_i \mathbf{v}^{l-1} - \boldsymbol{\epsilon}_x \langle \mathbf{v}^{l-1}, \boldsymbol{\epsilon}_x \rangle - \boldsymbol{\epsilon}_y \langle \mathbf{v}^{l-1}, \boldsymbol{\epsilon}_y \rangle - \boldsymbol{\epsilon}_z \langle \mathbf{v}^{l-1}, \boldsymbol{\epsilon}_z \rangle + \widetilde{\mathbf{b}}_i, \tag{46}$$

where $i = (1, 2, \cdots, N_s)$. Note that equation (23) of Scheme 1 and equation (46) of Scheme 2 can be constructed and solved in parallel to enhance the computational efficiency.

Numerical results obtained show that the velocity field has a zero sum (i.e., $< 10^{-8}$) in each direction as the scheme is designed to do so. Also, as expected, the centre of mass is observed to be stationary (i.e. $|x_c|, |y_c| < 10^{-10}$).

4 Numerical examples

The proposed two schemes are verified in 2D flows: Couette flows, flows past a periodic square array of cylinders and particulate suspensions. The flows are modelled using a DPD system in two dimensions with the following standard parameters: $a_{ij} = 18.5$, $n = 4$, $\sigma = 3$, $r_c = 1$ and $k_B T = 1$. Cutoff radius and Boltzmann temperature are commonly normalized to unity. Repulsion parameter a_{ij} is chosen from the requirement that the DPD fluid is supposed to have the same isothermal compressibility to that of water. For the modelling of single phase systems, DPD is known to possess a scale-free property over the whole mesoscopic range. The larger the number of fluid molecules packed into a DPD particle (larger DPD particle), the higher the coarse graining level will be. With an appropriate scaling scheme, numerical results from solving the DPD equations of motion can be independent to the number density chosen. The noise level $\sigma = 3$ is recommended as its larger values may render the system unstable. Under these values, fast simulations ($\Delta t = O(10^{-3}) - O(10^{-2})$) can be achieved [4]. In the present work, we employ a time step in the range of 0.005 to 0.01 and observe that the temperature is maintained constant. In solving the velocity DPD equation, the Picards iteration is carried out without relaxation for the fastest convergence.

4.1 Couette flow

This example is chosen to study the performance of Scheme 1 and Scheme 2. Consider a flow in the space between two horizontal parallel plates, $L_x \times L_y = 10 \times 10$. The two plates are sliding in opposite directions of a speed $U = 10$. We impose periodic boundary conditions on the left and right boundaries of the flow domain and the velocity $\mathbf{U} = (\pm U, 0)^T$ on the wall frozen particles. Before the simulation is started, the DPD particles are allowed to equilibrate from a uniform configuration and initial velocities are chosen in such a way that their sums in all directions are zero. Both Scheme 1 and Scheme 2 are employed. Figure 2 shows Scheme 2 converges much faster than Scheme 1 for a given time step. With a given tolerance of 10^{-7}, the Picard algorithm typically requires about 2100 iterations for Scheme 1 and about 450 iterations for Scheme 2. The ratio of the CPU time required for Scheme 1 to that of Scheme 2 is about 3.65. Figure 3 displays the distribution of number density and velocities on the flow cross section by Scheme 2. It can be seen that an approximately linear velocity profile is obtained. In Figure 4, we compare the development of the $x-$component velocity profile between two cases: $m = 0$ (overdamped) and $m = 1$ (standard), revealing that the DPD fluid in the overdamped limit has a much faster dynamic response.

4.2 Flow past a periodic square array of fixed cylinders

This example is chosen to investigate compressibility of the overdamped DPD system. Because of periodicity, one can replace the infinite domain with a finite one containing only one cylinder to analyse the flow (Figure 5). Assume that the motion of a fluid is driven by a pressure drop in the x direction. Using Fourier series, Hasimoto [14] derived an analytic expression for the drag on a cylinder in a periodic arrangement,

$$F = \frac{4\pi\eta U}{\ln(h/a) - 1.3105 + \cdots}, \tag{47}$$

where U is the mean velocity in the x direction, a the cylinder radius and h the centre-to-centre distance between two adjacent cylinders. If the denominator is approximated by the first two terms as shown above, estimation (47) can be used for the case of dilute arrays of

cylinders.

Figure 5 shows an initial configuration of the DPD system for the reduced domain. We take the domain size as 6×6 and model a cylinder by using 4 fixed basic DPD particles placed at vertices of the square whose side length is 0.1. Boundary conditions are all periodic on the outer faces of the computational domain. Figure 6a shows a contour plot of the radial component of the repulsive/conservative force field caused by fixed particles representing the cylinder, i.e., $\sum_{i=1}^{4} a_{ij}(1 - r_{ij}/r_c)\mathbf{e}_{ij} \cdot \mathbf{e}_{oj}$ (o the centre of the cylinder). Figure 6b shows an exclusive zone of circulate shape generated in no flow simulation, where image resolution is based on 10×10 bins per unit area. It is thus possible to use a few DPD particles to represent a cylinder, which appears to be more effective and efficient than the way of placing much larger numbers of DPD particles on the surface of a cylinder (further discussion will be given in the next example). We utilise the radial distribution function

$$g(q) = \frac{1}{N/A} \frac{s}{2\pi q \Delta q}, \tag{48}$$

to measure the exclusion size, where A is the area of the domain containing N particles and s is the number of particles in a circular shell of width $q \to (q + \Delta q)$ at a distance q from the centre of the cylinder. Using $\Delta q = 0.01$, an exclusion zone of radius $a \approx 0.25$ corresponding to the area, where $g(q) < 0.001$, is estimated.

To verify the proposed method, we apply an external force $\mathbf{P} = (P, 0)^T$ to each particle inside the simulation domain and then measure the total force on the cylinder exerted by the solvent particles. Consider P in the range of 0.1 to 1 with an increment of 0.1. Figure 7 shows the drag forces obtained by the analytic solution (47) and present simulation. Note that the present drag forces are computed at $m = 0$ and thus at $Re = 0$. A very good agreement is achieved for small mean flow velocities (small external forces). At large external forces, the computed values are a bit lower than the analytic ones, probably due to compressibility that will be numerically investigated next.

As remarked earlier, the Mach number is dependent on the particle mass, mean flow velocity, etc. We consider two values of m: 0 (strongly overdamped DPD) and 1 (standard DPD),

and investigate the variation in number density, measured through

$$\frac{1}{N_b}\sqrt{\sum_{i=1}^{N_b}(n_i - n)^2}, \tag{49}$$

where N_b is the number of bins in the fluid region and n_i the calculated number density in bin i. This may be regarded as a measure of compressibility. Results obtained are shown in Figure 8. With increasing external force, the residual in number density of the unit mass case grows much faster than in the case of zero mass (for the external force increasing from 0.1 to 1, this compressibility measure increases by 3.10 times for $m = 1$ and only 1.16 times for $m = 0$). Regarding the variation in divergence of velocity ($\nabla.\mathbf{u}$), the behaviour is similar. As the external force changes from 0.1 to 1, the increase in $\nabla.\mathbf{u}$ is 4.60 times for $m = 1$ and only 1.41 times for $m = 0$. The overdamped limit clearly promotes incompressibility.

4.3 Particulate suspensions

A suspended particle of spherical/circular shape can be modelled using a single DPD particle [15-19,8] or a set of frozen DPD particles [20-23]. The single particle model involves three groups of DPD parameters: the first group associated with the interactions between solvent-solvent particles, the second with solvent-colloidal particles and the third with colloidal-colloidal particles. They all need be defined in advance; more effort is required for the second group, particularly for the case of polydispersed suspensions (colloidal particles having a size distribution). The frozen particle model requires a relatively large number of DPD particles on the surface to represent a colloidal particle, resulting in systems of larger size for a given volume fraction. The position and velocity of a colloidal particle are advanced according to the Newton-Euler equation. The present work is concerned with the modelling of massless suspended particles (cylinders). We propose to use a set of only three basic DPD particles (referred to here as "constituent particles") to represent a colloidal particle, in which they are connected together via springs (Figure 9a). The stiffness of springs is chosen to be large but still maintaining the fluctuating motion part of these DPD particles (constituent particles). Consequently, the motion of a colloidal particle is also updated using DPD equation, which avoids difficulties faced by solving Newton-Euler equation with zero mass. Let α and β

denote a pair of constituent particles of a colloidal particle. The velocity DPD equations for the particles α and β become

$$\sum_{j=1,j\neq\alpha}^{N}(\mathbf{F}_{\alpha j,C}+\mathbf{F}_{\alpha j,D}+\mathbf{F}_{\alpha j,R})-H(r_{\alpha\beta}-\overline{r}_{\alpha\beta})\frac{\mathbf{r}_{\alpha\beta}}{r_{\alpha\beta}} = \mathbf{0}, \tag{50}$$

$$\sum_{j=1,j\neq\beta}^{N}(\mathbf{F}_{\beta j,C}+\mathbf{F}_{\beta j,D}+\mathbf{F}_{\beta j,R})+H(r_{\alpha\beta}-\overline{r}_{\alpha\beta})\frac{\mathbf{r}_{\alpha\beta}}{r_{\alpha\beta}} = \mathbf{0}, \tag{51}$$

where H is the stiffness of springs and $\overline{r}_{\alpha\beta}$ the reference length (the initial length of the spring). The proposed model only involves DPD parameters of the fluid case and one extra parameter, namely the stiffness of springs, which can be easily chosen. Constituent particles of the colloids are basically the same as solvent particles since they are all subject to the same values of DPD parameters including the thermodynamic temperature. In this regard, the volume fraction can be simply defined as $\phi = N_c^0/(N_s + N_c^0)$, where N_s is the number of basic particles used to represent the solvent phase and N_c^0 the number of basic particles used to model the colloidal phase.

Our computational domain is taken as 6×6. With $n = 4$, there are 144 free DPD particles used to represent the fluid phase. An illustration of the spatial configuration of the DPD system at an instant time is shown in Figure 9b. We employ a shear rate in the range of 0.25 to 33 and spring stiffness $H = 1000$. Figure 10 displays the radial component of the conservative force field generated by three basic particles that are located at the vertices of an equilateral triangle with $\overline{r}_{\alpha\beta} = 0.25$. We utilise expression (48) to measure the size of particles, resulting in a nearly zero size ($a < 0.01$) for a solvent particle and $a \approx 0.2$ for a colloidal particle (Figure 11). We observe that the spring forces on the constituent particles of the colloidal particle are oscillatory with zero mean and they thus do not make any contributions to the stress tensor. The self diffusion D is measured by means of mean squared displacement (MSD)

$$D = \frac{1}{4}\lim_{t\to\infty}\frac{d}{dt}\langle|\mathbf{r}_i(t)-\mathbf{r}_i(0)|^2\rangle, \tag{52}$$

which is calculated in ensemble-average sense for the solvent particle and time-average sense for the colloidal particle. They result in $D = 0.095$ for the former and $D = 0.055$ for the

latter. The self diffusion is seen to reach a stable stage very quickly. In the solvent case, the MSD curves contain some fluctuations, probably due to the combination of zero mass (i.e., no inertial forces) and small particle size. The Péclet number is defined as $Pe = \dot{\gamma}a^2/D$, where $\dot{\gamma}$, a and D are the shear rate, radius and diffusion coefficient of a suspended particle, respectively. This number measures the relative importance of dissipative (hydrodynamic contribution) and random (random contribution) forces.

For 2D dilute suspensions, the relative/reduced viscosity, which is the ratio of the effective viscosity of the suspension to that of the suspending fluid, has been shown to be [24]

$$\eta_r = (1 + 2\phi)\,, \tag{53}$$

where ϕ is the volume fraction. We employ several sets of colloids: (1,2,3,4,6,8), corresponding to volume fraction in range of 0.0204 to 0.1429. Figure 12 shows good agreement between the present relative viscosities and those predicted by (53) as ϕ approaches zero. We observe a decrease in viscosity with increasing Péclet number (i.e., shear thinning) for low values of ϕ as shown in Figure 13.

5 Concluding remarks

We investigate the behaviour of strongly overdamped DPD systems in modelling the interaction between fluid and solid objects. Two iterative numerical schemes are proposed for solving the resultant sparse DPD system at each time step. With the presence of frozen particles in wall regions, a relative representation of particle motion with respect to the centre of mass is a better means to model the flow - in this representation, the artifacts due to the reaction forces are eliminated. In addition, the inclusion of the physical velocity constraint of the mass centre into the DPD system significantly enhances the efficiency of the iterative solving process. Solid objects of circular shape can be modelled using 3 or 4 basic DPD particles only. Results obtained for flows in periodic arrays of cylinders and particulate suspensions at a dilute/semi-dilute regime and zero Reynolds number agree well with those predicted by theories. It is clear that the overdamped limit promotes incompressibility and

improves the dynamic response of the DPD fluid, allowing creeping flows of complex fluids (suspension, emulsion, polymer solution, polymer melt, etc.) to be effectively modelled.

Acknowledgement

This work is supported by The Agency for Science, Technology and Research (A*STAR) through grant #102 164 0145. N. Mai-Duy also would like to thank the Australian Research Council for an ARC Future Fellowship (FT0990768).

References

1. P.J. Hoogerbrugge, J.M.V.A. Koelman, Simulating microscopic hydrodynamic phenomena with dissipative particle dynamics, Europhysics Letters. 19(3) (1992) 155-160.

2. P. Español, P. Warren, Statistical mechanics of dissipative particle dynamics, Europhysics Letters. 30(4) (1995) 191-196.

3. P. Español, Hydrodynamics from dissipative particle dynamics, Phys. Rev. E. 52 (1995) 1734-1742.

4. R.D. Groot, P.B. Warren, Dissipative particle dynamics: Bridging the gap between atomistic and mesoscopic simulation, J. Chem. Phys. 107 (1997) 4423.

5. C. Marsh, Theoretical aspect of dissipative particle dynamics (PhD Thesis), University of Oxford, 1998.

6. D. Pan, N. Phan-Thien, N. Mai-Duy, B.C. Khoo, Numerical investigations on the compressibility of a DPD fluid, Journal of Computational Physics. 242 (2013) 196-210.

7. X.J. Fan, N. Phan-Thien, S. Chen, X. Wu, T.Y. Ng, Simulating flow of DNA suspension using dissipative particle dynamics, Phys. Fluids. 18(6) (2006) 063102.

8. N. Mai-Duy, D. Pan, N. Phan-Thien, B.C. Khoo, Dissipative particle dynamics modelling of low Reynolds number incompressible flows, J. Rheol. 57(2) (2013) 585.

9. N. Phan-Thien, N. Mai-Duy, D. Pan, B.C. Khoo, Exponential-time differencing schemes for low-mass DPD systems, Computer Physics Communications. 185(1) (2014) 229-235.

10. N. Mai-Duy, N. Phan-Thien, B.C. Khoo, A numerical study of strongly overdamped Dissipative Particle Dynamics (DPD) systems, Journal of Computational Physics. 245 (2013) 150-159.

11. N. Phan-Thien, Understanding Viscoelasticity: An Introduction to Rheology, second Edition, Springer-Verlag, Berlin, 2013.

12. E. Bodewig, Matrix Calculus, North-Holland Publishing, Amsterdam, 1956.

13. N. Phan-Thien, S. Kim, Microstructures in Elastic Media: Principles and Computational Methods, Oxford University Press, New York, 1994.

14. H. Hashimoto, On the periodic fundamental solutions of the Stokes equations and their application to viscous flow past a cubic array of spheres, Journal of Fluid Mechanics. 5(2) (1959) 317-328.

15. W. Dzwinel, D.A. Yuen, A two-level, discrete-particle approach for simulating ordered colloidal structures, Journal of Colloid and Interface Science. 225(1) (2000) 179-190.

16. V. Pryamitsyn, V. Ganesan, A coarse-grained explicit solvent simulation of rheology of colloidal suspensions, J. Chem. Phys. 122 (2005) 104906.

17. W. Pan, I.V. Pivkin, G.E. Karniadakis, Single-particle hydrodynamics in DPD: A new formulation, EPL. 84(1) (2008) 10012.

18. W. Pan, B. Caswell, G.E. Karniadakis, Rheology, microstructure and migration in Brownian colloidal suspensions, Langmuir. 26(1) (2010) 133-142.

19. M. Whittle, K.P. Travis, Dynamic simulations of colloids by core-modified dissipative particle dynamics, J. Chem. Phys. 132 (2010) 124906.

20. J.M.V.A. Koelman, P.J. Hoogerbrugge, Dynamic simulations of hard-sphere suspensions under steady shear, Europhysics Letters. 21(3) (1993) 363-368.

21. E.S. Boek, P.V. Coveney, H.N.N. Lekkerkerker, P. van der Schoot, Simulating the rheology of dense colloidal suspensions using dissipative particle dynamics. Phys. Rev. E. 55(3) (1997) 3124-3133.

22. N.S. Martys, Study of a dissipative particle dynamics based approach for modeling suspensions, J. Rheol. 49 (2005) 401.

23. S. Chen, N. Phan-Thien, B.C. Khoo BC, X.-J. Fan, Flow around spheres by dissipative particle dynamics, Phys. Fluids. 18(10) (2006) 103605.

24. J.F. Brady, The Einstein viscosity correction in n dimensions, International Journal of Multiphase Flow. 10(1) (1984) 113-114.

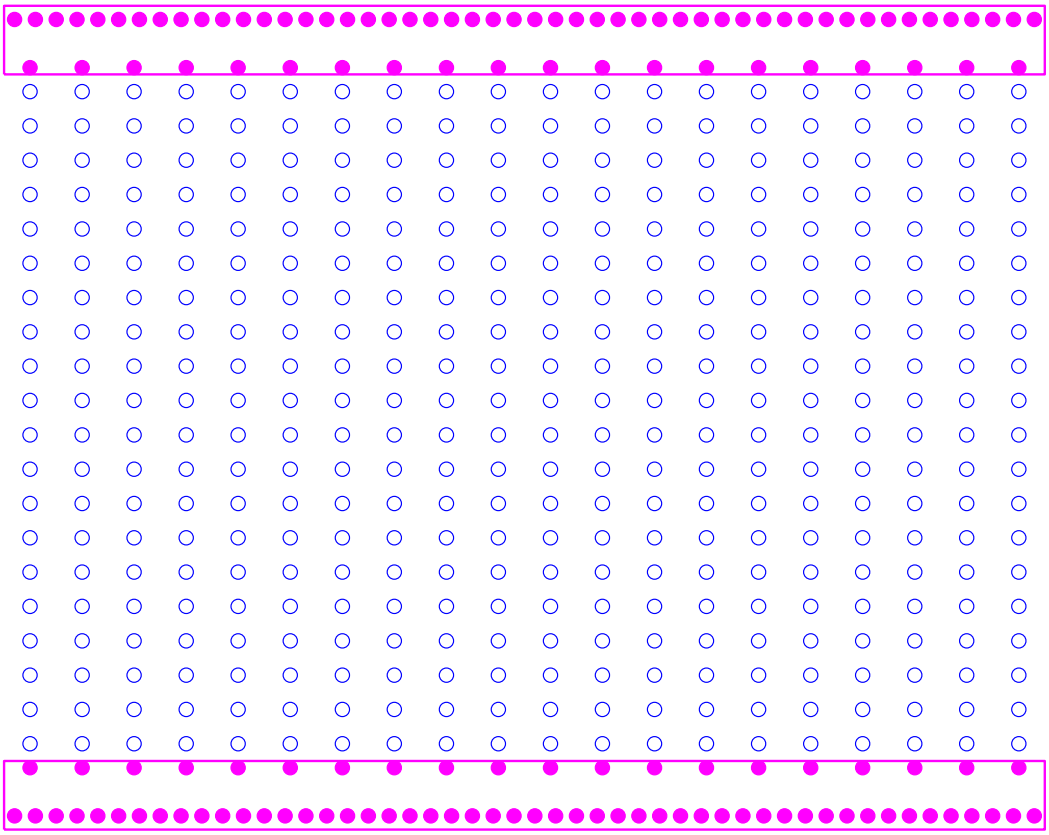

Figure 1: A DPD system and its initial configuration: fluid modelled by blue particles and solid walls modelled by magenta particles.

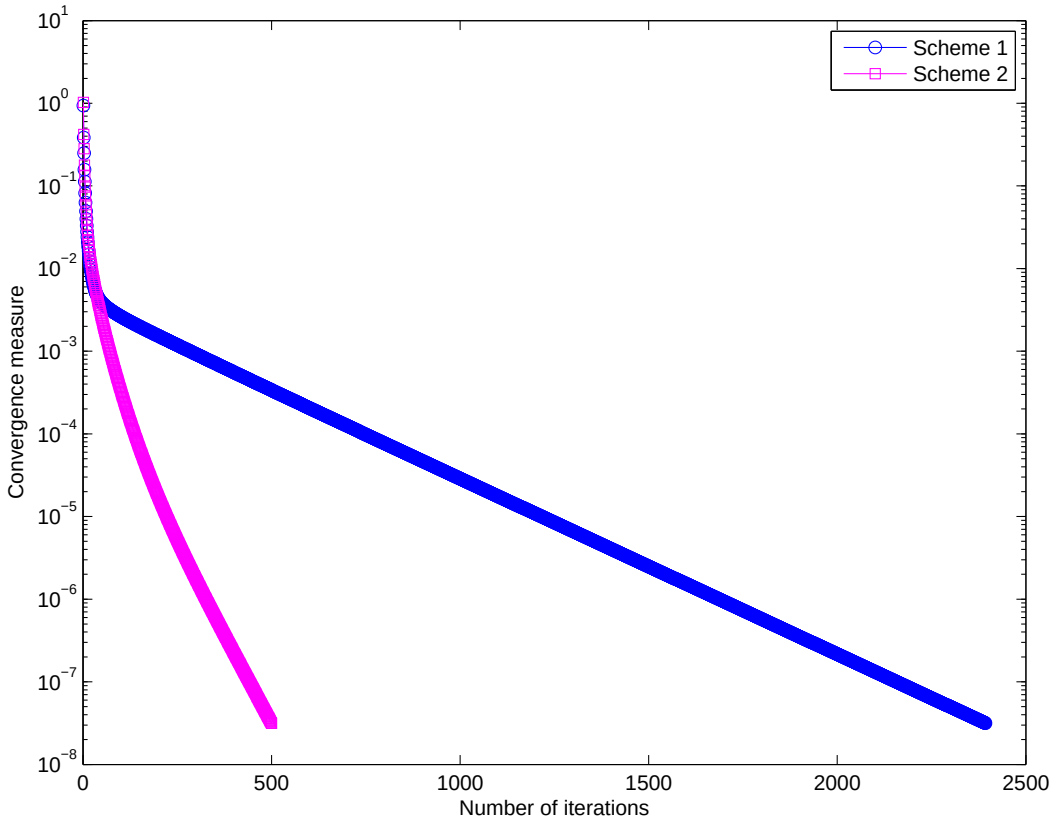

Figure 2: Couette flow: Scheme 2 converges much faster than Scheme 1. Given a tolerance of 10^{-7}, the Picard algorithm typically requires about 2100 and 450 iterations for Scheme 1 and Scheme 2, respectively.

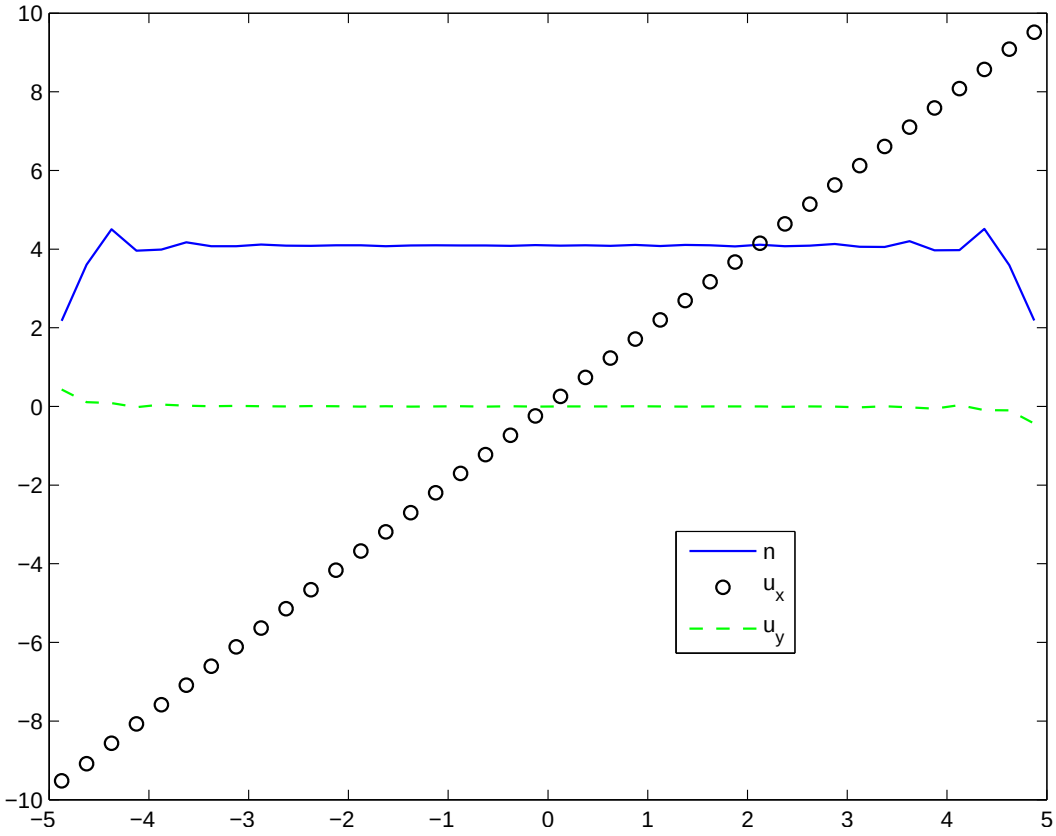

Figure 3: Couette flow, $L_x \times L_y = 10 \times 10$, $\Delta t = 0.01$: variations of number density and velocities on the flow cross section by Scheme 2.

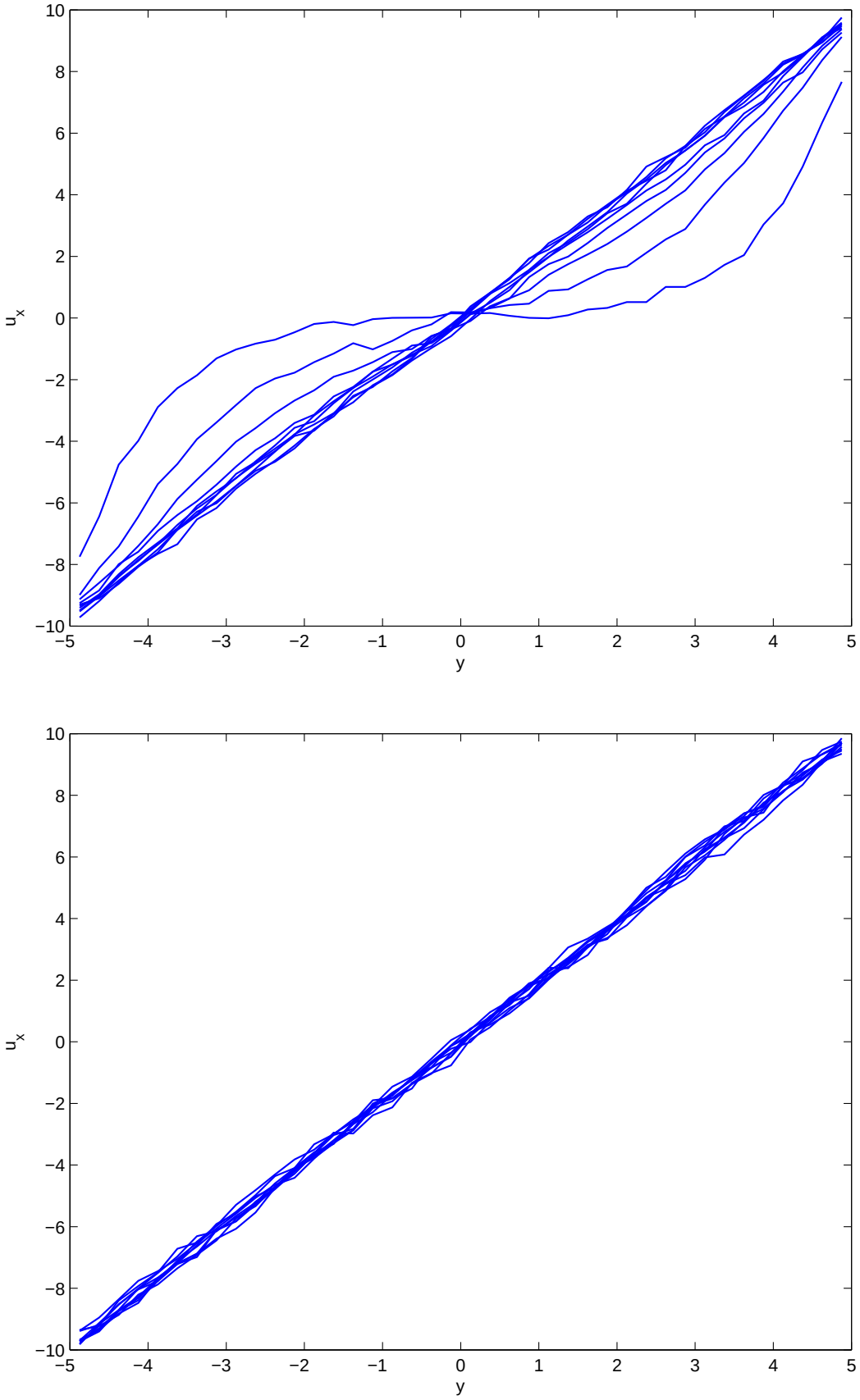

Figure 4: Couette flow, $\Delta t = 0.01$, 2000 time steps: Developments of velocity profile in two cases: $m = 1$ (top) and $m = 0$ (bottom), where results are displayed at time levels $(2, 4, \cdots, 20)$. The latter has a faster dynamic response.

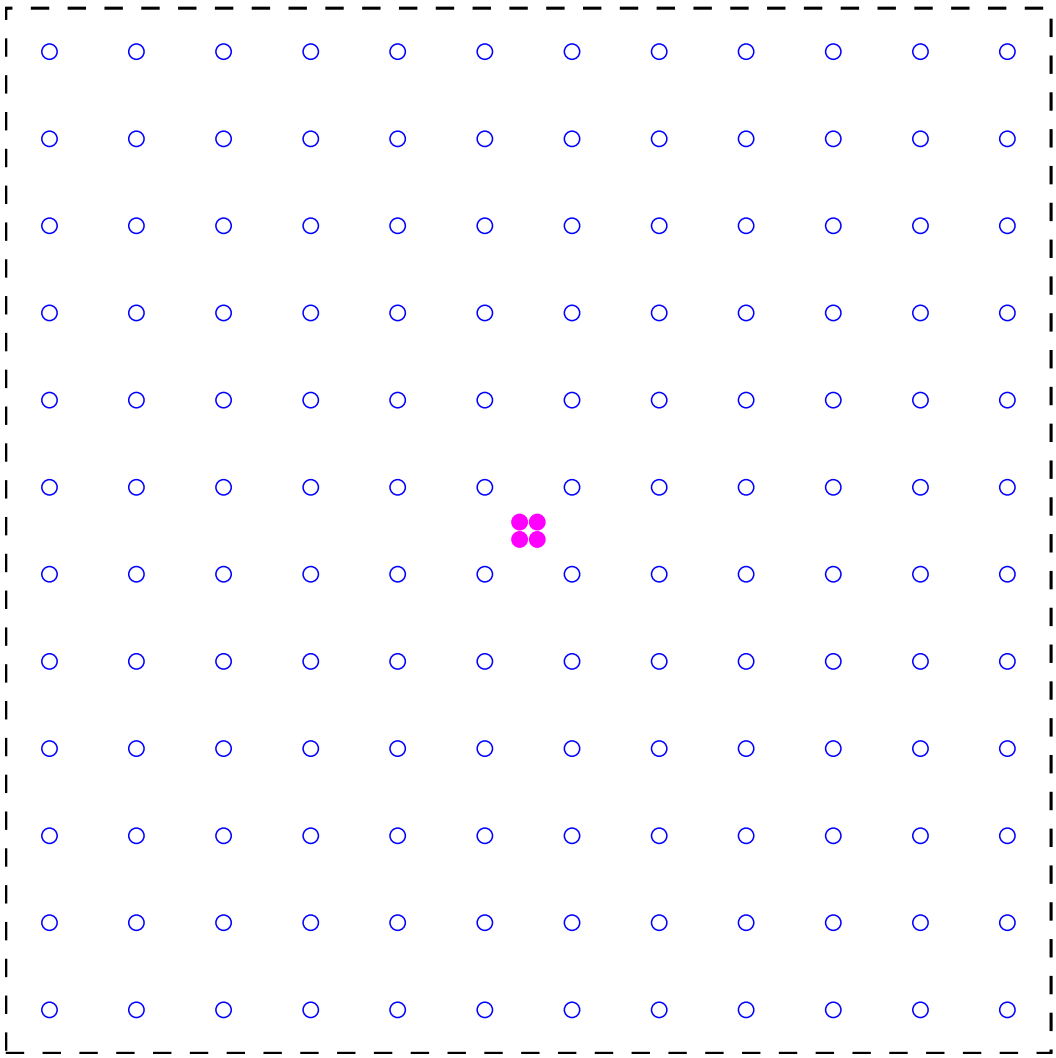

Figure 5: Flow past a periodic square array of cylinders: Initial configuration (fluid represented by blue particles and cylinder by magenta particles).

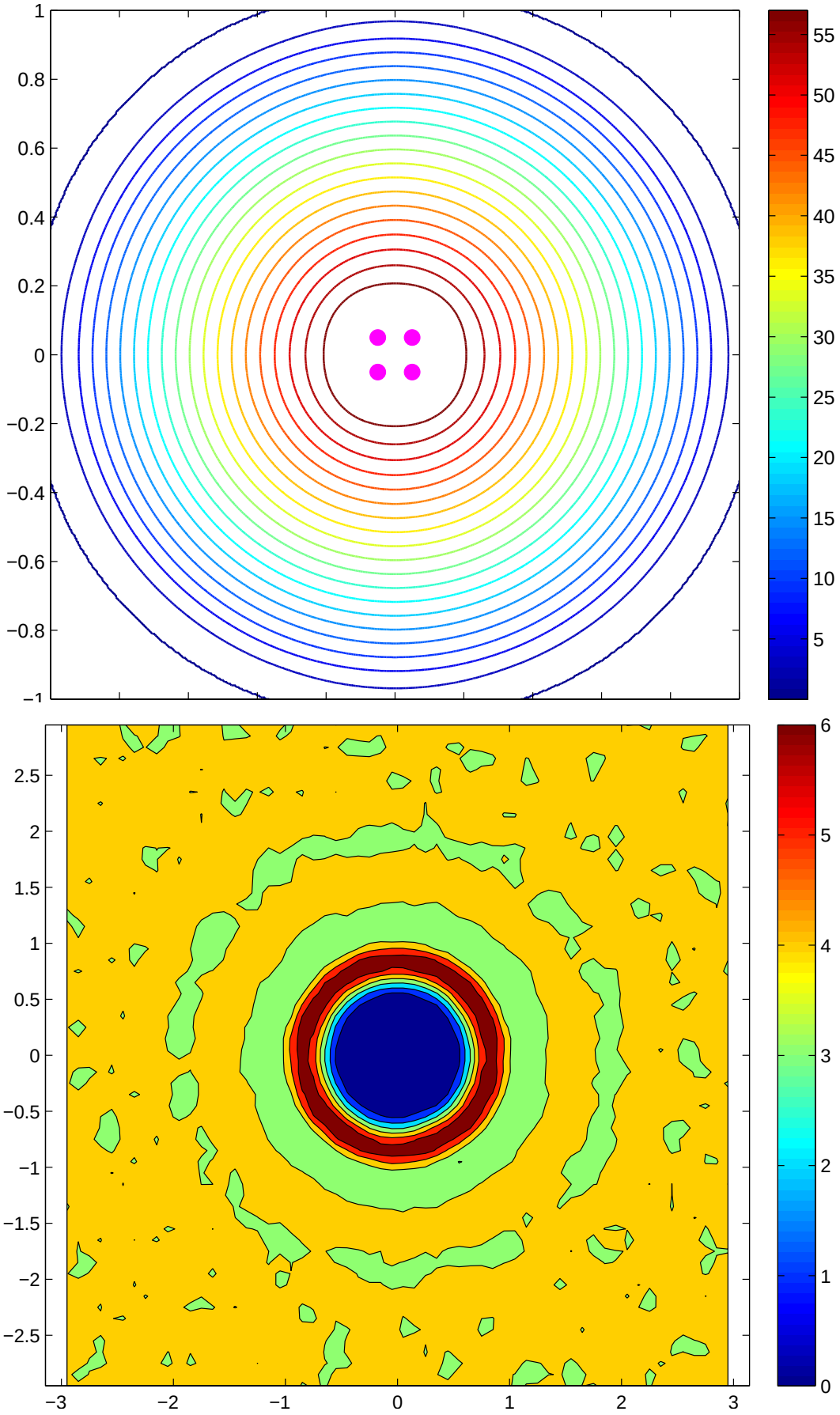

Figure 6: Flow past a periodic square array of cylinders. Top: repulsion force field by four constituent particles representing a cylinder. Bottom: number density distribution, clearly showing an exclusion zone of circular shape ($n = 0$) at the center.

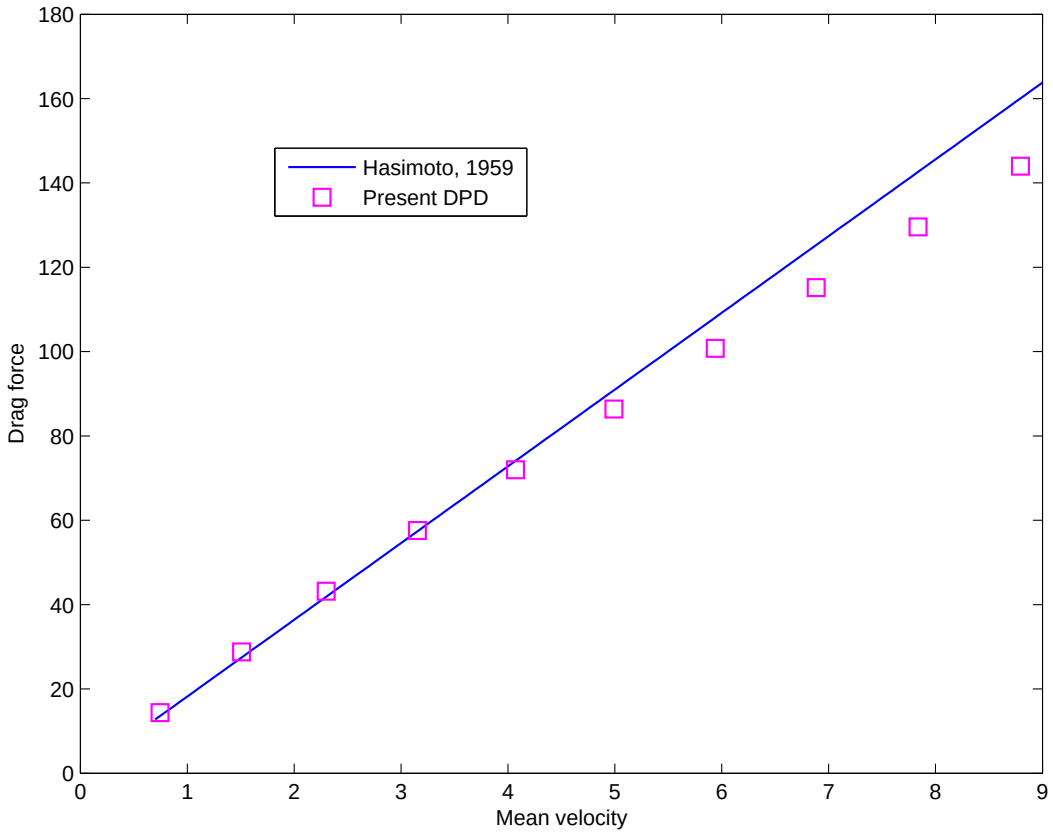

Figure 7: Flow past a periodic square array of cylinders: drag force on a cylinder is plotted as function of mean flow velocity. Analytical results by Hasimoto [14] (solid line) are also included.

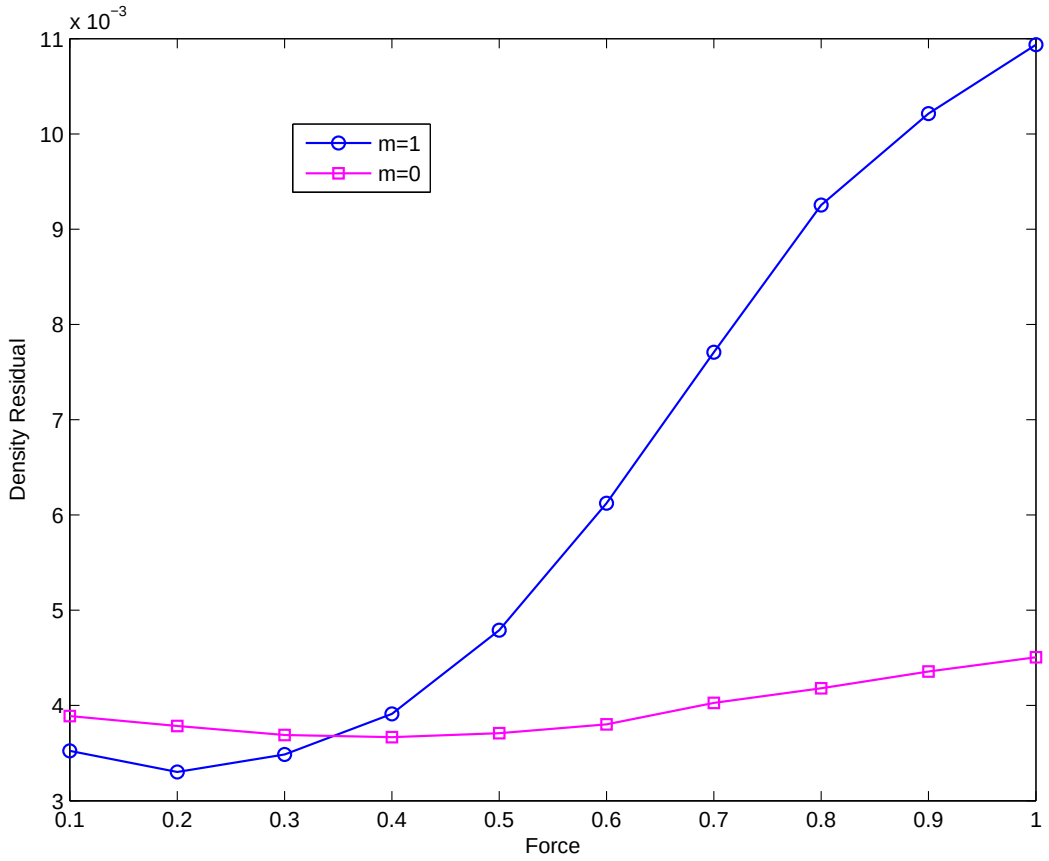

Figure 8: Flow past a periodic square array of cylinders: Residual of number density versus external force for two cases: $m = 0$ and $m = 1$. They are measured over the domain excluding the circular region of unit radius at the centre. Variation in number density in the overdamped limit is much smaller.

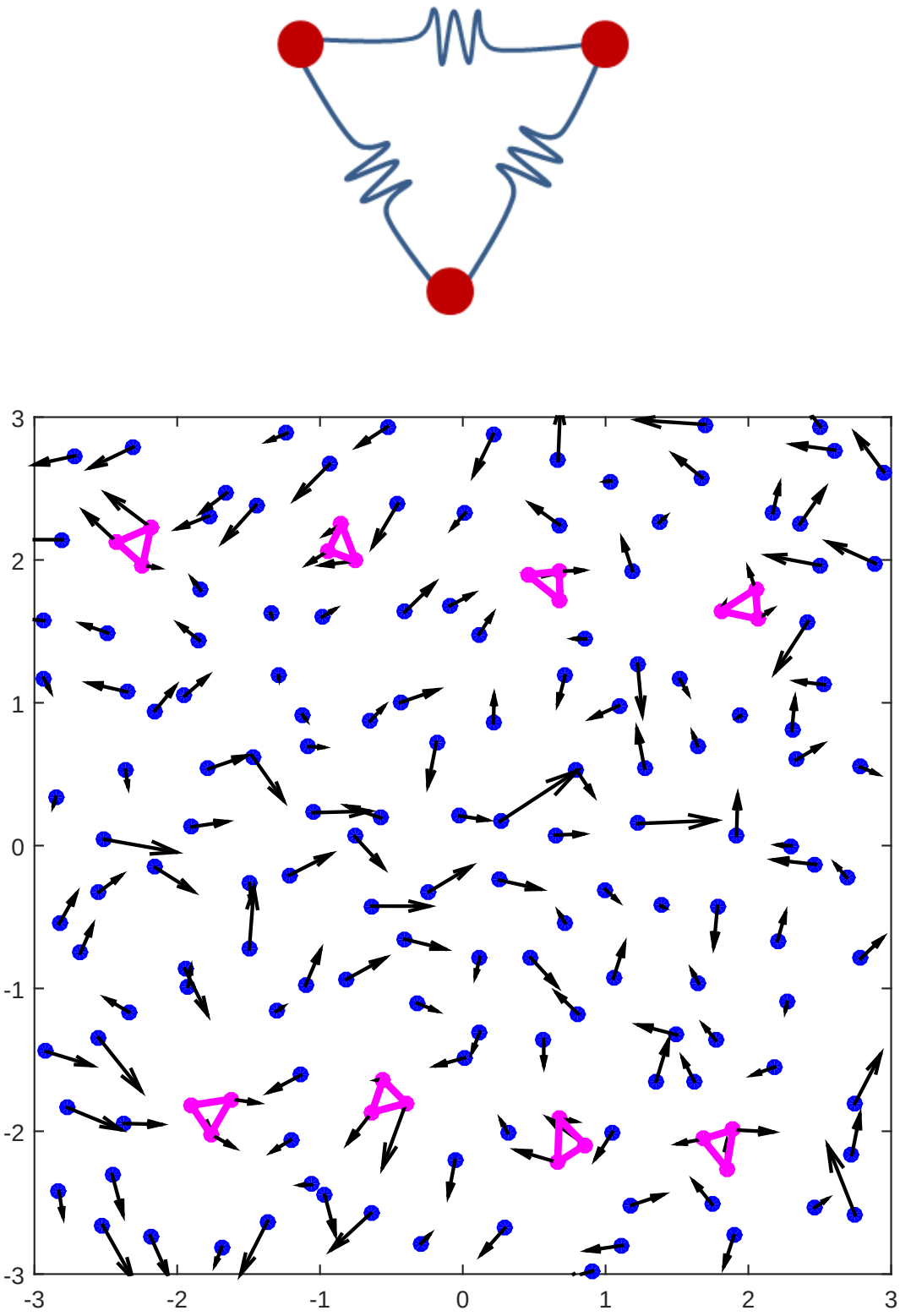

Figure 9: Particulate suspensions: a spring model for suspended particles (top) and an illustration of spatial configuration of the DPD system at an instant time (flow domain of 6×6, 144 solvent particles in blue colour, 8 suspended particles in magenta and velocity vector in black) (bottom).

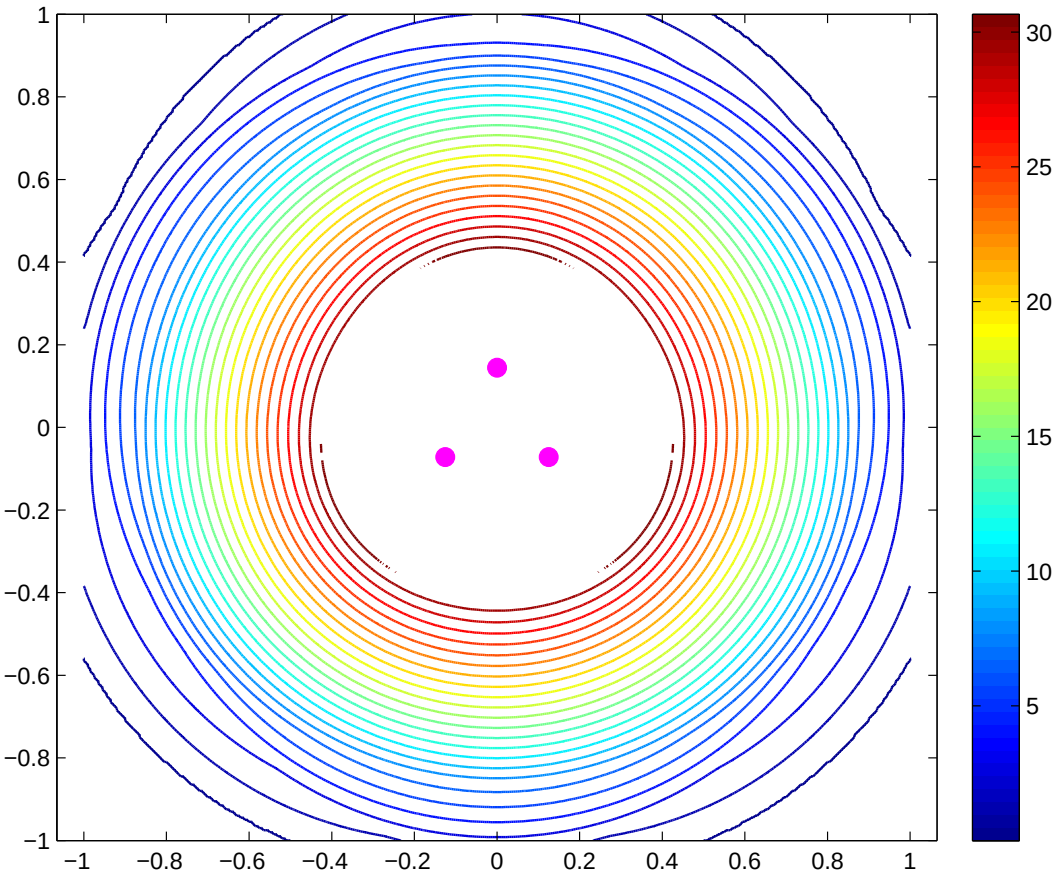

Figure 10: Particulate suspensions: the radial component of conservative force field generated by three constituent particles of a colloidal particle.

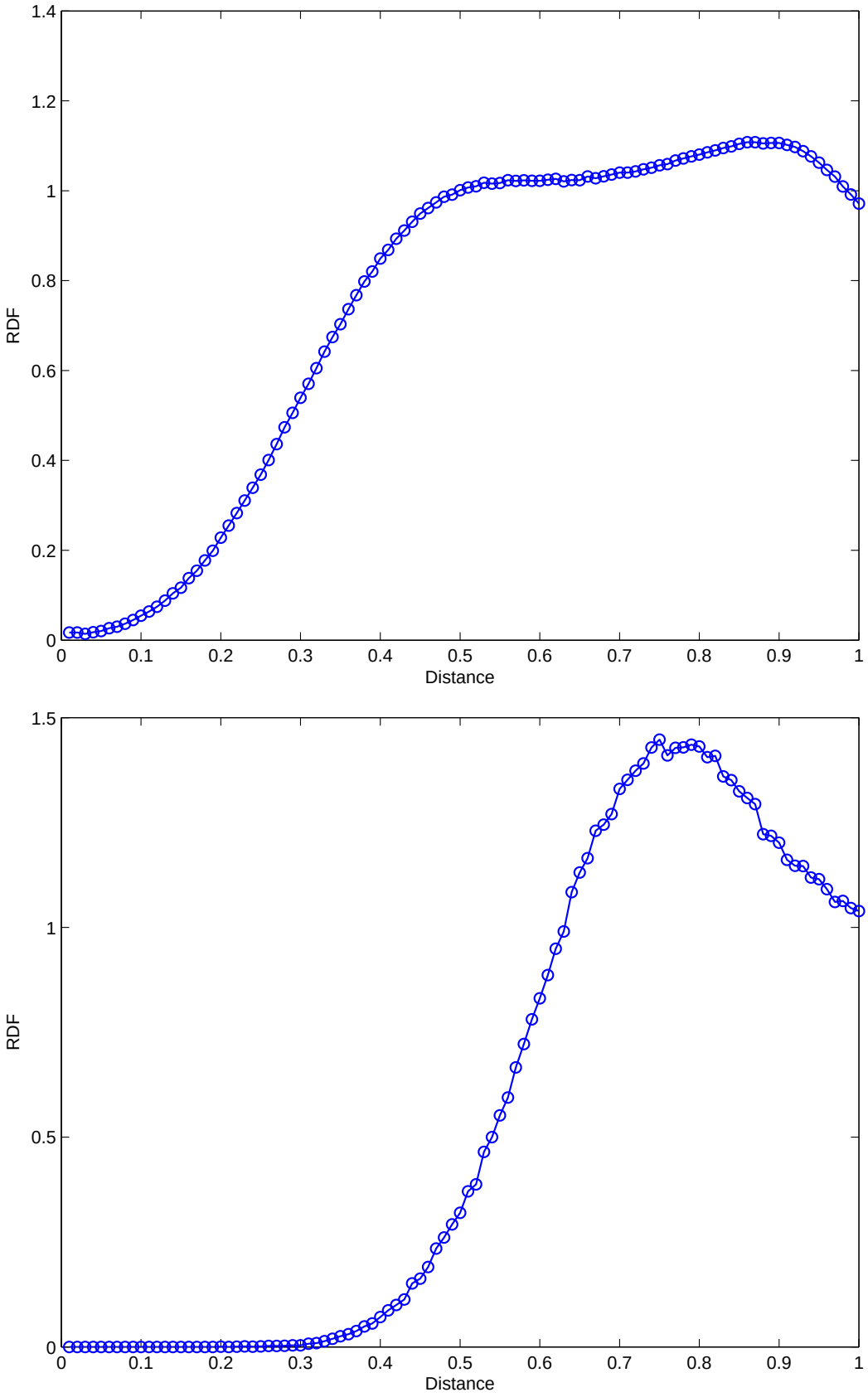

Figure 11: Particulate suspensions, no flow simulation, $\Delta t = 0.005$: radial distribution functions for the solvent (top) and colloidal (bottom) particles.

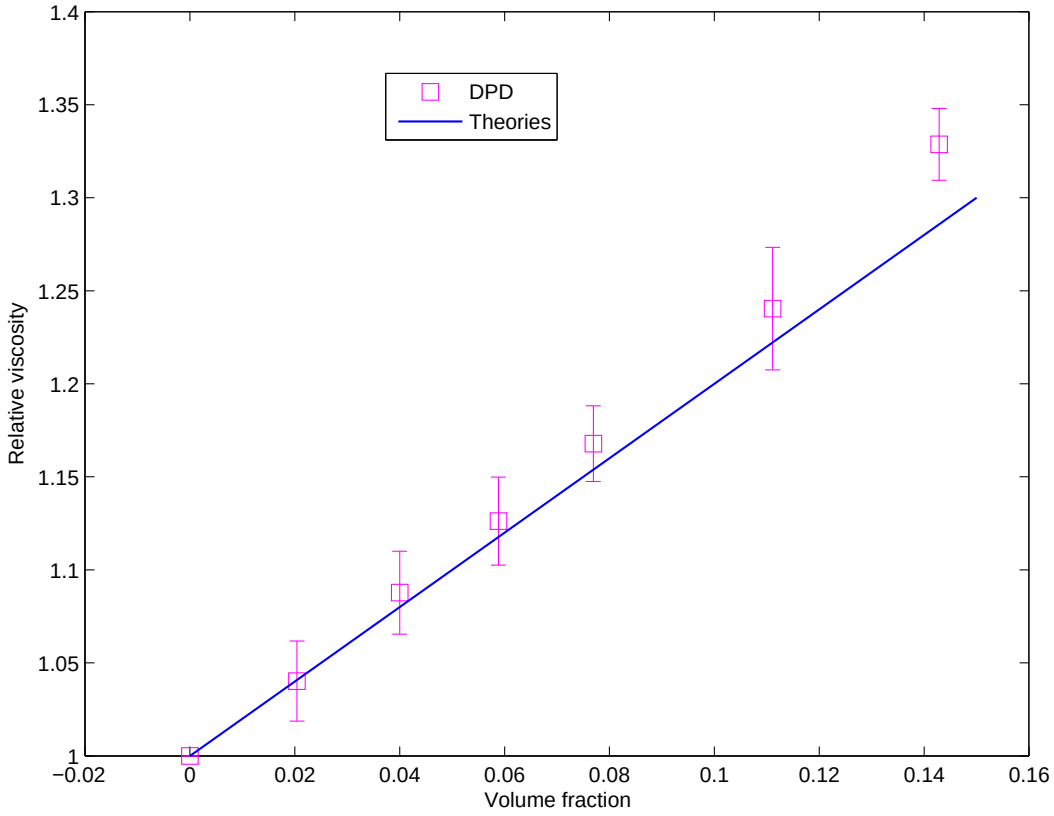

Figure 12: Particulate suspensions: relative viscosity versus volume fraction in dilute and semi-dilute regimes. As the volume fraction approaches zero, the present DPD results are in good agreement with the theoretical prediction for a dilute regime (i.e. Equation (53)).

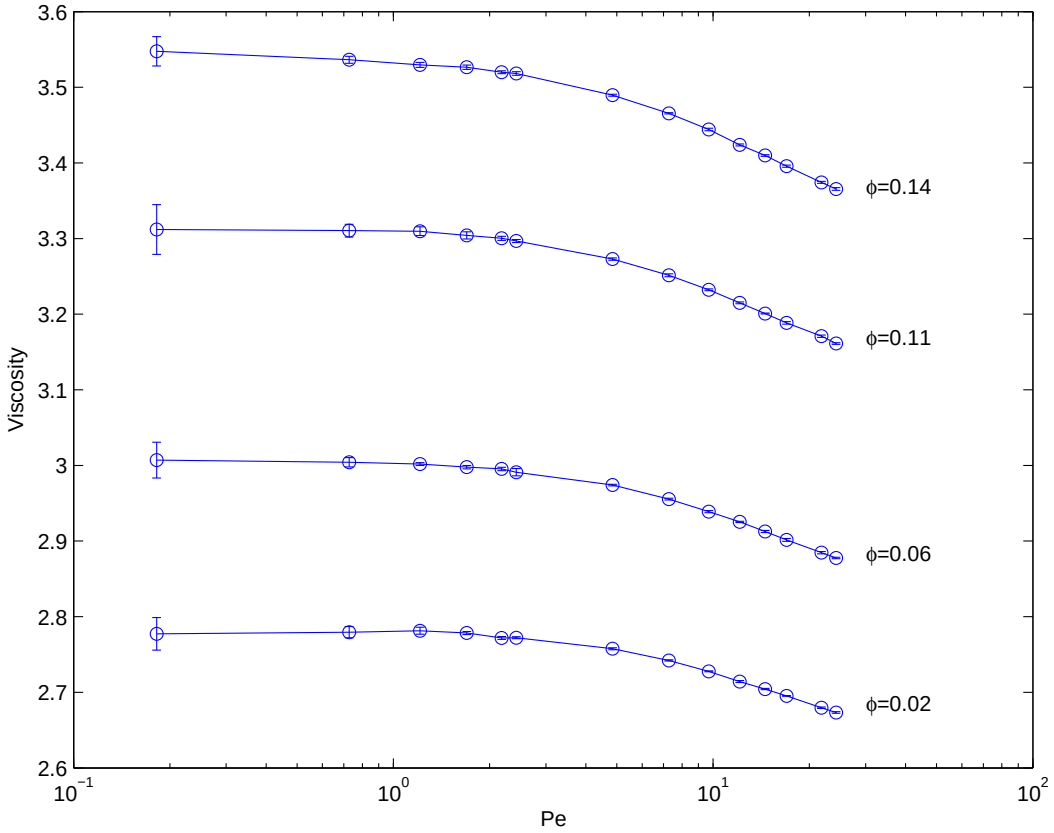

Figure 13: Particulate suspensions: viscosity versus Péclet number for low volume fractions, showing shear thinning behaviour.